PAPER

Check for updates

In situ self-assembly of zirconium metal–organic frameworks onto ultrathin carbon nitride for enhanced visible light-driven conversion of CO₂ to CO†

Yanan Wang, [ID] [a] Wenlong Zhen,[b] Yiqing Zeng,[a] Shipeng Wan,[a] Haiwei Guo,[a] Shule Zhang [ID] *[a] and Qin Zhong*[a]

A series of Zr-porphyrin metal–organic framework (Zr-PMOF)/ultrathin g-C₃N₄ (UCN) (ZPUCN) heterostructure photocatalysts, as stable and efficient catalysts for the photoreduction of CO₂, have been fabricated *via* a facile *in situ* hydrothermal self-assembly method. An interfacial interaction is formed due to hollow Zr-PMOF nanotubes being surrounded by 3D ultrathin g-C₃N₄ (UCN) and benefiting from the ultrathin and conjugated π-structure of UCN, the unsaturated metal atoms and organic ligands of Zr-PMOFs can covalently link to organic g-C₃N₄. The interaction provides a platform for UCN as a conductor to transfer e⁻ or as a donor to transfer e⁻ to Zr–O cluster active sites to catalyze CO₂, substantially achieving the spatial separation of charge carriers and suppressing the photogenerated electron–hole (e⁻–h⁺) pair recombination rate. Benefitting from the cooperative effects of the well-designed nanostructure and chemical grafting, in the absence of triethanolamine, cocatalysts and photosensitizers, the optimized ZPUCN hybrid not only exhibits a better CO evolution yield (5.05 μmol g⁻¹ h⁻¹), which is 2.2 times and 3.2 times higher than those of pure Zr-PMOFs and UCN, respectively, but also displays excellent stability after 96 h photocatalysis. Information about the mechanism is also elucidated from selected characterizations.

1. Introduction

The levels of carbon dioxide (CO_2), one of the greenhouse gases, have been increasing steadily over the past century with the combustion of fossil fuels and expansion in the activities of humankind.[1–3] Due to global industrialization, global warming and limited fossil fuels are unavoidable problems that people have to face. One promising and sustainable strategy to effectively and simultaneously solve these two environmental pollution and energy crisis problems is the chemical conversion of CO_2 to valuable chemical fuels through photocatalytic CO_2 reduction by inexhaustible solar energy.[4] However, the artificial photoreduction CO_2 is still challenging due to the huge kinetic and thermodynamic barrier of CO_2 and the sluggish reaction kinetics for producing solar fuels.[2] The development of highly effective photocatalysts is the key to boost the photoreduction process. Since the first investigation on TiO_2 for CO_2

photoreduction, many inorganic semiconductor photocatalysts have been explored and studied. Most reductive inorganic semiconductors including TiO_2,[5] WO_3,[6] ZnO,[7] and Zn_2GeO_4 (ref. 8) are UV light-responsive ones, which restricts the utilization of solar energy for the photocatalytic process.

Metal–organic frameworks (MOFs), as a new family of photocatalytic materials, has exhibited outstanding catalytic performance due to their porous framework structures, easy functionalization, high designability and high surface area.[9] Extensive reports have indicated that MOFs such as UiO-based MOFs,[10] MIL-based MOFs[11] and PCN-based MOFs[12,13] are excellent materials to photo-reduce CO_2. Among them, porphyrin metal–organic frameworks (PMOFs), as a member of PCN-based MOFs, are porous coordination materials with metalloporphyrin-based linkers interconnected by metal ions or metal carboxylate cluster secondary building units. Metalloporphyrin and their derivatives are well-known for improving many biological functions, especially light harvesting. Thus, some issues in the photocatalytic process (*e.g.*, light harvesting) can be solved by using metalloporphyrins as MOF linkers.[14–16] However, the photocatalytic efficiency of pure PMOFs is still unsatisfactory generally due to the fast combination of photoexcited electron–hole (e⁻–h⁺) pairs, which is related to the energy-level alignment flaws and asymmetry. Tremendous

[a]School of Chemical Engineering, Nanjing University of Science and Technology, Nanjing 210094, PR China. E-mail: zq304@njust.edu.cn; shulezhang@163.com; Fax: +86 25 84315517; Tel: +86 25 84315517

[b]School of Materials Science and Engineering, Nanyang Technological University, 50 Nanyang Avenue, Singapore 639798, Singapore

efforts such as doping,[17] tuning morphology,[18] and coupling with other semiconductors[1,19] have been devoted to boost the migration rate. Among them, constructing a heterojunction is one of the most effective strategies to address e^-–h^+ recombination in recent years.[20] In particular, the effective spatial separation of charge carriers can be achieved when two semiconductors have suitable energy levels, consequently suppressing the bulk and surface recombination.[21] For instance, Zheng synthesized 0D/2D carbon nitride quantum dot/porphyrin MOFs for increasing photocatalytic CO_2 reduction. Ye *et al.* developed UiO-66/2D g-C_3N_4 nanosheet heterostructures for CO_2 photoreduction.[22] Xiong *et al.* designed g-C_3N_4 nanotube/ZIF-8 composites to enhance CO_2 conversion efficiency.[23] However, the examples of PMOF-based heterojunction photocatalysts for CO_2 reduction are insufficient. Graphitic carbon nitride (g-C_3N_4) has triggered great attention in diverse fields due to its nontoxicity, high stability, and low cost.[24,25] Notably, the suitable structure (bandgap $E_g = 2.7$ eV, energy potential of the conduction band $E_{CB} = -1.3$ eV *vs.* NHE) makes it an important player in the field of photocatalytic CO_2 reduction and hydrogen generation.[23,26] In addition, g-C_3N_4 with a pliable framework can effortlessly anchor or enclose on another material, thus constructing an intimate contact interface.[27] More importantly, as a metal-free conjugated polymer semiconductor, the purely organic nature of g-C_3N_4 plays a key role to couple with MOFs.

Herein, ultrathin 3D g-C_3N_4 was implemented to decorate hollow Zr-PMOF nanotubes to build a novel hybrid photocatalyst (ZPUCN-*x*, *x* is the actual mass of the addition of UCN) under mild reaction conditions to cooperatively convert CO_2. This work aims to make full use of the complementary features of Zr-PMOFs and g-C_3N_4 to achieve the spatial separation of charge carriers, suppressing the photogenerated electron–hole (e^-–h^+) pair recombination rate. Benefitting from the cooperative effects of the well-designed nanostructure and chemical grafting, the optimized ZPUCN heterojunctions boost charge transport and light harvesting, therefore presenting high photocatalytic CO_2 reduction efficiency. 3D ultrathin g-C_3N_4 (UCN) exhibits superiority compared with the bulk g-C_3N_4 (BCN) fabricated by melamine. Based on the calculated energy band positions, the plausible enhanced mechanism for the Zr-PMOFs/UCN composite was also proposed in detail.

2. Results and discussion

2.1. Structure and morphology

The XRD patterns of UCN, Zr-PMOFs, and ZPUCN composites are shown in Fig. 1. The typical peak of UCN at 27.4 indexed to the (002) plane is detected, corresponding to the typical stacked graphite-like structure (JCPDS no. 87-1526). For comparison, the XRD pattern of bulk carbon nitride (BCN) was characterized. As shown in Fig. 1a, there are two typical peaks around 13.1° (100) and 27.6° (002) for BCN. The negative shift in the (002) peak for UCN compared with that for BCN is due to the loosely layered structure.[28] In addition, less prominent and broader typical peaks are related to the smaller length of interlayer periodicity, indicating that UCN possesses smaller interlayer periodicity and larger layered spacing.[29] SEM was carried out to further contrast pure BCN and UCN (Fig. S3a and b†). Unlike the tightly stacked bulk BCN, UCN exhibited ultrathin and loosely stacked nanoflakes, which enhanced the specific surface area and provided abundant active sites for anchoring other materials and surface redox reactions. The consistent XRD pattern of Zr-PMOFs with those reported previously[12] indicates that Zr-PMOFs have been successfully synthesized. For the ZPUCN-*x* composites, the *in situ* grafting of Zr-PMOFs on UCN had no obvious effect on the crystal structure. The characteristic peaks of Zr-PMOFs remained for all ZPUCN hybrids except for slight differences in the peak intensity, indicating that more UCN species were introduced into the ZPUCN-*x* composites. The unique peaks of UCN were not found due to the relatively low peak intensity or/and low content.

2.2. Photocatalytic activity

Photocatalytic CO_2 reduction studies were implemented in a customized glass system without any cocatalysts or electron donors under visible light. CO was detected as the only gas product, as shown in Fig. 2a. Bare BCN or UCN was not active to reduce CO_2 under this system, and the CO evolution rates were only 0.30 μmol h^{-1} g^{-1} and 1.59 μmol h^{-1} g^{-1}, respectively. Besides, there were traces of CH_4 (0.19 μmol h^{-1} g^{-1}) in UCN (Fig. S4†). Zr-PMOFs showed moderate CO_2 reduction with a CO evolution rate of 2.32 μmol h^{-1} g^{-1}. However, the ZPUCN-*x* heterojunction photocatalysts showed enhanced CO_2
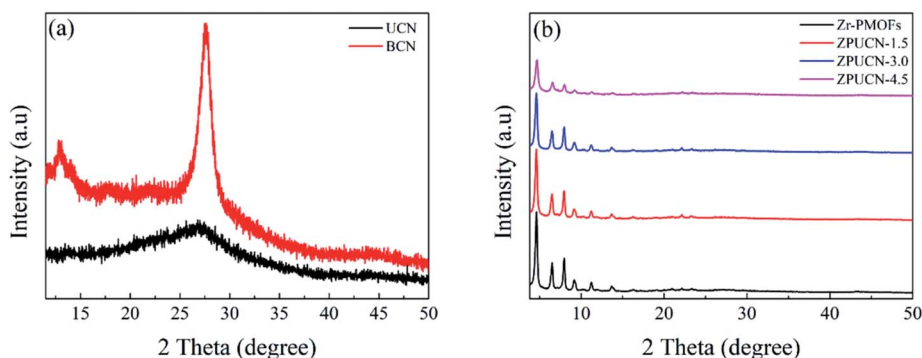

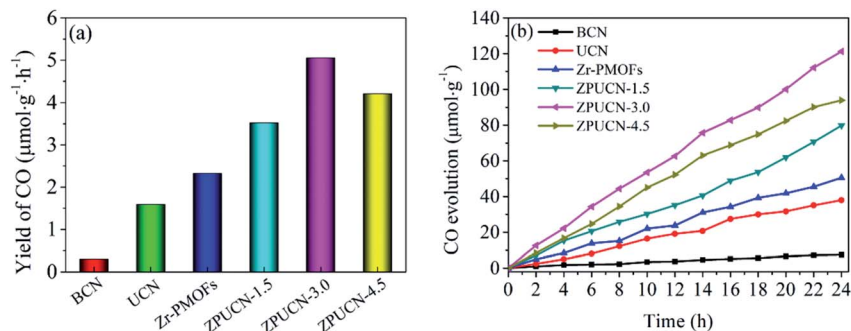**Fig. 1** XRD patterns of (a) UCN and BCN, (b) Zr-PMOFs and ZPUCN-*x*.

Fig. 2 (a) CO_2 photoreduction activities of different samples. (b) Time−yield plots of products.

photoreduction performance. Strikingly, ZPUCN-3 manifested a higher CO_2-to-CO conversion rate of 5.05 µmol h^{-1} g^{-1} even in the absence of any sacrificial agent, cocatalyst, and photosensitizer, which was about 3.2 times and 2.2 times higher than those of pure UCN and Zr-PMOFs, respectively. Meanwhile, the ZPUCN-3 hybrids also presented durable photoreduction CO_2 performance during consecutive photoreactions for 96 h (Fig. S4†), providing an accumulated CO yield of ca. 4.89×10^2 µmol g^{-1}. The remarkable CO_2 reduction performance of ZPUCN-x should be related to the unique heterostructures that

can accelerate the separation and transfer of photoinduced carriers. To exclude the possibility that the carbon source of CO was from acetonitrile or ZPUCN-x photocatalysts, a blank experiment was carried out in the presence of N_2 instead of CO_2 under the same conditions; no CO product was detected, demonstrating that the C species of CO originated from CO_2. The potential products generated in the liquid phase were detected by another gas chromatography equipped by a head-space sample injector and GC-MS. However, no HCHO, CH_3OH, and HCOOH were detected in the obtained liquid. Generally,
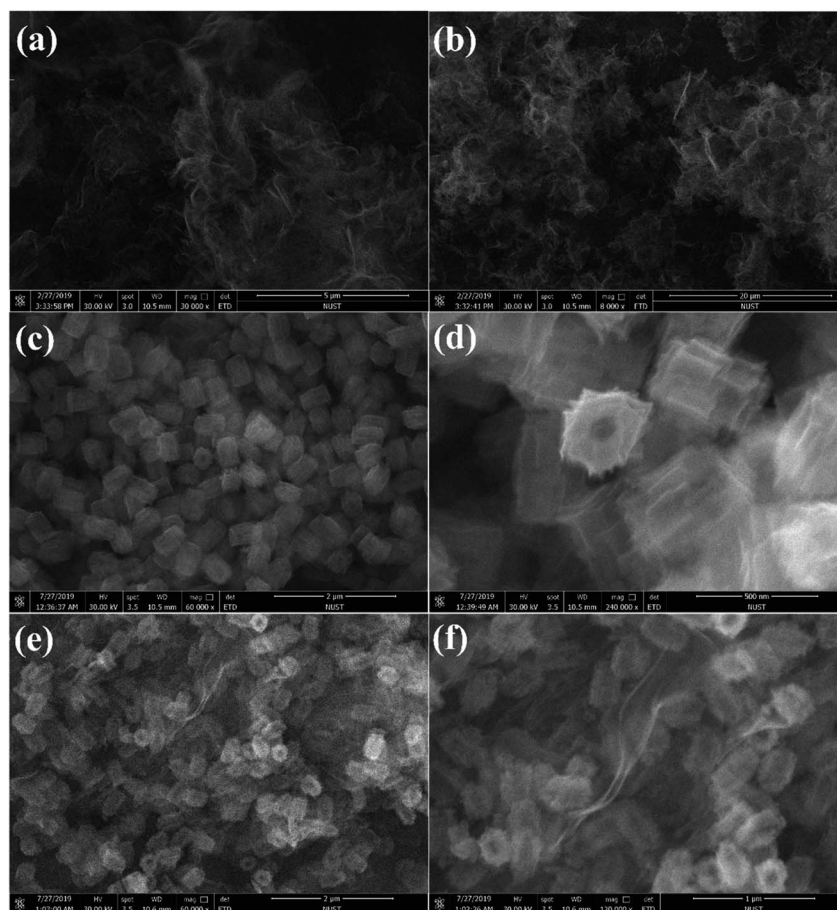

Fig. 3 Typical SEM images of (a and b) UCN, (c and d) Zr-PMOFs and (e and f) ZPUCN-3 composites.
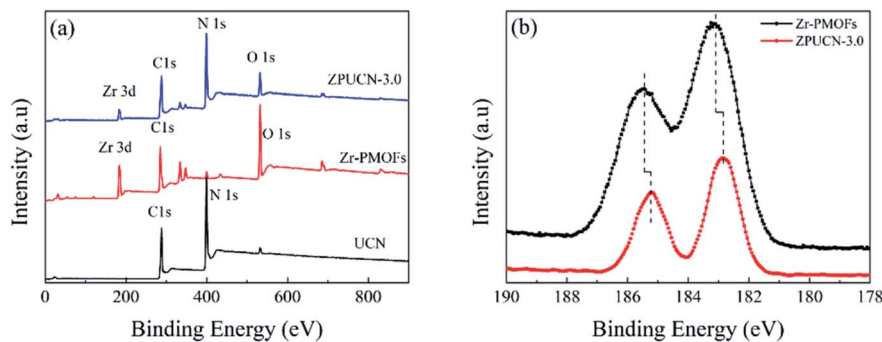
Fig. 4 (a) XPS survey spectra of UCN, Zr-PMOFs, and ZPUCN-3.0. (b) High-resolution XPS spectra of Zr 3d of Zr-PMOFs and ZPUCN-3.0.

the products of the photoreduction of CO_2 are HCOOH, CO, HCHO, CH_3OH, and CH_4, and the reduction potentials are -0.67 V, -0.52 V, -0.49 V, -0.40 V and -0.25 V, respectively.[30] However, only CO was detected in the present work, indicating good photocatalytic selectivity, which may be due to the following reasons: (i) the photoreduction of CO_2 tends to undergo proton-coupled electron transfer, but the amount of H_2O is too low to favor a hydrogenation reaction under this experimental condition. (ii) The reduction of CO_2 to CO needs 2 protons, while 4, 6, and 8 electrons are required to reduce it to HCHO, CH_3OH, and CH_4, respectively. (iii) The reduction potential for the formation of CO is moderate. In addition, the cyclic stability of CO evolution on the ZPUCN-3.0 hybrid structures was tested. As shown in Fig. S5,† the CO yield does not decline obviously after five photoreduction cycles. Furthermore, Fig. S6† displays that no obvious changes in the crystal structure can be observed in the XRD patterns of fresh and used ZPUCN-3.0.

The SEM images of pure UCN reveal that the 3D ultrathin structure is composed of cross-linked wrinkled or wavy nanoscale crystal layers (Fig. 3a and b). Uniform Zr-PMOF prisms were prepared by a solvothermal reaction. Fig. 3c shows that the average diameter and length of the Zr-PMOF prisms are about 200 nm and 400 nm, respectively. The magnified image shows that Zr-PMOFs are composed of well-organized assembled ultrathin nanosheets (Fig. 3d). By visualizing the morphology of the ZPUCN-3 composites (Fig. 3e and f), the Zr-PMOF prisms are surrounded by hierarchical UCN. No freestanding Zr-PMOF prisms were observed, which indicated that the growth of the Zr-PMOF prisms was precisely confined to the surface of UCN, resulting in the formation of a heterostructure interface. For comparison, the Zr-PMOF/BCN (ZPBCN) composite was prepared in a similar way except that UCN was used instead of BCN, as shown in Fig. S7.† By contrast, the SEM images show that Zr-PMOFs are evenly dispersed and prefer to enclose on the surface of UCN because of the loose lamellar structure, resulting in a strong interaction between Zr-PMOFs and UCN. Overall, the SEM information verifies the formation of heterojunctions and suggests an interfacial interaction between Zr-PMOFs and UCN. To further prove the interaction, XPS was performed, as shown in Fig. 4. The main peaks observed were those for C 1s and N 1s for pure UCN and C 1s, N 1s, O 1s, and Zr 3d for Zr-

PMOFs (Fig. 4a). The XPS survey spectrum of ZPUCN-3.0 shows all of the above-mentioned elements. With respect to the peak for Zr 3d of Zr-PMOFs (Fig. 4b), two characterized peaks at 184.75 eV and 182.43 eV corresponded to Zr $3d_{3/2}$ and Zr $3d_{5/2}$, verifying the presence of Zr^{4+} ions. By contrast, the Zr 3d binding energy of ZPUCN-3.0 had a negative shift to 184.45 eV and 182.14 eV, indicating the existence of interactions between UCN and Zr-PMOFs.

2.3. Optical and electrochemical properties

UV-vis diffuse reflectance spectroscopy (DRS) was carried out to obtain optical information.[31] To a great extent, the electronic structure of g-C_3N_4 can be tuned by the design of a nanostructure. Accordingly, the adsorption edge of UCN has a significant redshift from ~450 nm (BCN) to ~650 nm, which is mainly due to nanoscale effects.[32] Furthermore, compared with the result for BCN, longer tail absorption from 550 nm to 800 nm was observed for UCN, which should result from the abundant defects in UCN. Zr-PMOFs can efficiently harvest visible light due to the H_2TCPP ligand as a visible light absorption unit (shown in Fig. 5). After UCN incorporation, a slight reduction in the light harvesting capacity was observed for ZPUCN-x versus Zr-PMOFs, which should be related to the surface coating of UCN. However, more importantly, it was
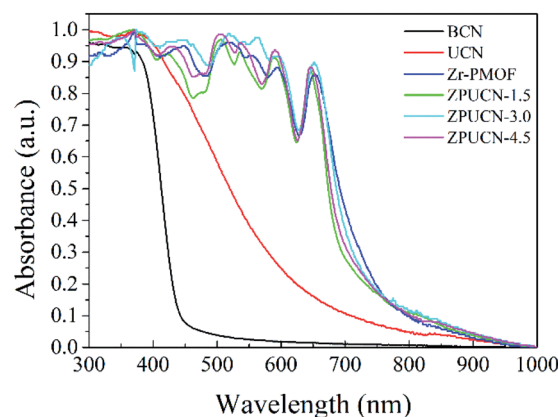

Fig. 5 UV-vis diffuse reflectance spectra of as-synthesized pure BCN, UCN, Zr-PMOFs, and ZPUCN-x.
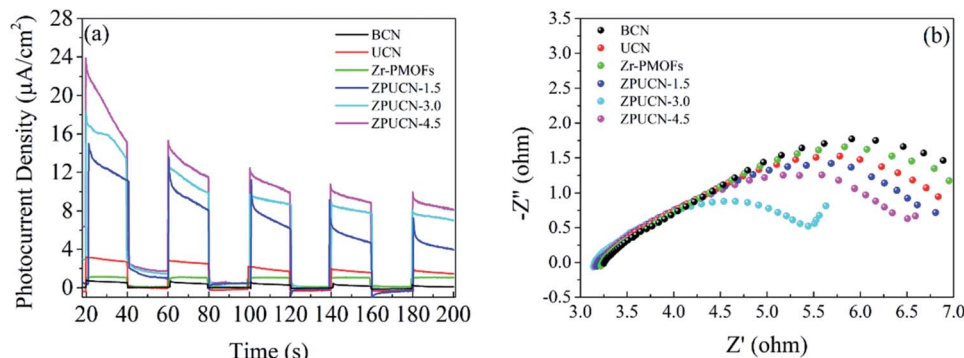
Fig. 6 (a) Transient photocurrent response; (b) the EIS Nyquist plots of BCN, UCN, Zr-PMOFs, and ZPUCN-x.

verified that the ultrathin porous layer could be integrated on Zr-PMOFs without weakening the light absorption ability by *in situ* synthesis.

Generally, the separation efficiency of photogenerated charge is a critical factor affecting photocatalytic activities. Photoelectrochemical measurements were obtained to further study the interface separation and migration properties of photoinduced charge carriers. As shown in Fig. 6a, the ZPUCN-x heterojunctions show enhanced photocurrent intensity to different extents compared with pure UCN and Zr-PMOFs during the switching on of visible light. The high photocurrent response of the ZPUCN-x heterojunctions should be owing to the lower recombination rate of the photoinduced $e^-–h^+$ pairs in the hybrid structures. Electrochemical impedance spectroscopy (EIS) is also an efficient way to characterize the interfacial charge transfer; there is a strong negative correlation between the radius of the EIS curve and the charge transfer rate. As presented in Fig. 6b, the EIS Nyquist plots of the ZPUCN-x composites show a smaller radius than that of pure UCN and Zr-PMOFs. A smaller resistance leads to better conductivity and is favorable for the transmission of the photogenerated electrons. Note that the smallest radius for the ZPUCN-3.0 hybrids was in accordance with the result of the photocurrent test and CO_2 photoreduction performance. The current–time curve of the ZPUCN-3.0 composites is exhibited in Fig. S8† under continuous light illumination. The current density of ZPUCN-3.0 remained unchanged after 3600 s, suggesting good photoelectrochemical stability of ZPUCN-3, which was in accordance with the results of the stability test of CO_2 photoreduction.

In addition, photoluminescence (PL) emission spectra were obtained to further investigate the lifetime of the photogenerated charge carriers. As shown in Fig. 7, the photoluminescence of ZPUCN-3.0 is quenched obviously compared with that for Zr-PMOFs, indicating that the photoinduced charge recombination rate occurring in the hybrids has been greatly inhibited.[29,33] The efficient charge migration should be ascribed to the ZPUCN-3.0 heterojunction structure as two-step excitation and charge separation processes occur in the coupled system, in which the photogenerated e^- and h^+ migrate to two materials in opposite directions and achieve $e^-–h^+$ spatial separation.[34] Hence, ZPUCN-3.0 enables a long-lifetime e^- for
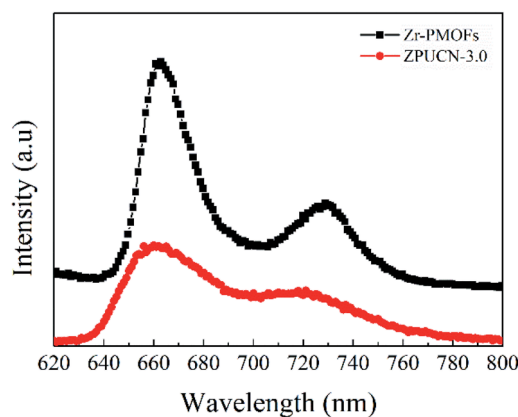

Fig. 7 Photoluminescence spectra of Zr-PMOFs and ZPUCN-3.0.

CO_2 photoreduction with a higher performance than pure Zr-PMOFs. This result also shows good agreement with the photoelectrochemical measurements discussed above.

2.4. Possible photocatalytic mechanism

A potential CO_2 photocatalytic mechanism for the ZPUCN-x system is proposed in Fig. 8. Based on the results of CO_2
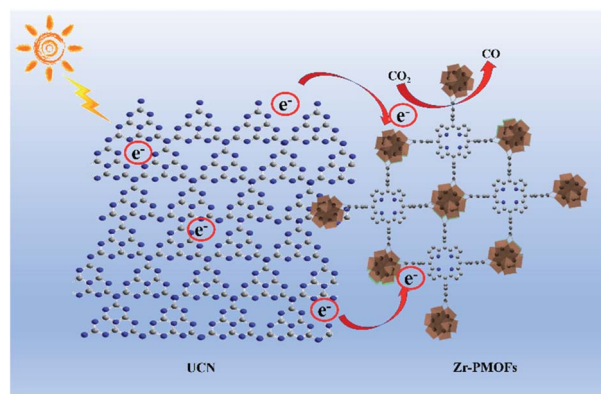

Fig. 8 Schematic illustration for the enhanced CO_2 photoreduction performance of coupled UCN and Zr-PMOFs under visible light irradiation.

6038 | *J. Mater. Chem. A*, 2020, **8**, 6034–6040

This journal is © The Royal Society of Chemistry 2020

photoreduction performance and characterizations, the mechanism information the photogenerated charge transfer between the interfacial phase mainly follow the typical heterojunction mechanism. Benefiting from the ultrathin and conjugated π-structure of UCN, the unsaturated metal atoms and organic ligands of Zr-PMOFs can be covalently linked to organic g-C_3N_4, leading to an interfacial interaction. The interfacial interaction provides a platform for UCN as a conductor to transfer e^- from ligands or transfer e^- to Zr–O cluster active sites to catalyze CO_2. Since Zr-PMOFs are capable of high CO_2 uptake, the enriched electrons would interact with the abundant CO_2 on Zr-PMOFs, facilitating photocatalytic efficiency. Moreover, more negative CB of UCN compared with that of Zr-PMOFs (Fig. S9†) could drive the transfer of e^-. As a result, the electron re-localization suppressed the recombination rates of photoexcited charge carriers in both UCN and Zr-PMOFs, which was in accordance with the photo-electrochemistry and PL results. In addition, as e^- donors, the photoinduced e^- generated on UCN would also react with CO_2 directly.

3. Conclusions

It was demonstrated that a series of ZPUCN-x hybrid structures were synthesized by a facile in situ solvothermal method, in which the Zr-PMOF nanotubes were surrounded by 3D ultrathin g-C_3N_4. Benefiting from the ultrathin and conjugated π-structure of UCN, the unsaturated metal atoms and organic ligands of Zr-PMOFs can be covalently linked to organic g-C_3N_4. The interfacial interaction provides a platform for UCN for transferring e^- to Zr–O clusters or as a conductor to transfer e^-, thus facilitating the separation and migration efficiency of the photoexcited charge carriers on the ZPUCN-x hybrids. In addition, in the absence of triethanolamine, cocatalysts, and photosensitizers, the optimized ZPUCN-3.0 composites exhibit a CO_2-to-CO conversion rate of 5.05 μmol g^{-1} h^{-1}, which is roughly 3.2 times and 2.2 times higher than those of pure UCN and Zr-PMOFs, respectively. It is important to note that the photocatalytic activity of the ZPUCN-3.0 composites has negligible decrease after 96 h photocatalysis; thus, they possess great potential for being implemented in highly efficient solar fuel conversion.

Conflicts of interest

There are no conflicts to declare.

Acknowledgements

References

1 Q. Mu, W. Zhu, X. Li, C. Zhang, Y. Su, Y. Lian, P. Qi, Z. Deng, D. Zhang and S. Wang, Appl. Catal., B, 2020, 262, 118144.

2 X. Li, J. Yu, M. Jaroniec and X. Chen, Chem. Rev., 2019, 119, 3962–4179.

3 R. Li, W. Zhang and K. Zhou, Adv. Mater., 2018, 30, e1705512.

4 L. Hao, L. Kang, H. Huang, L. Ye, K. Han, S. Yang, H. Yu, M. Batmunkh, Y. Zhang and T. Ma, Adv. Mater., 2019, 31, 1900546.

5 T. Inoue, A. Fujishima, S. Konishi and K. Honda, Nature, 1979, 277, 637–638.

6 L. Yang, B. Liu, T. Liu, X. Ma, H. Li, S. Yin, T. Sato and Y. Wang, Adv. Mater., 2017, 7, 5075–5080.

7 G. Mahmodi, Sol. Energy Mater. Sol. Cells, 2018, 111, 31–40.

8 J. Wang, Y. Asakura and S. Yin, Nanoscale, 2019, 11, 20151–20160.

9 T. Zhang and W. Lin, Chem. Soc. Rev., 2014, 43, 5982–5993.

10 Z. Zheng, H. Xu, Z. Xu and J. Ge, Small, 2018, 14, 1702812.

11 X. Li, Y. Pi, Q. Hou, H. Yu, Z. Li, Y. Li and J. Xiao, Chem. Commun., 2018, 54, 1917–1920.

12 H. Q. Xu, J. Hu, D. Wang, Z. Li, Q. Zhang, Y. Luo, S. H. Yu and H. L. Jiang, J. Am. Chem. Soc., 2015, 137, 13440–13443.

13 T. He, S. Chen, B. Ni, Y. Gong, Z. Wu, L. Song, L. Gu, W. Hu and X. Wang, Angew. Chem., Int. Ed., 2018, 57, 3493–3498.

14 M. C. So, G. P. Wiederrecht, J. E. Mondloch, J. T. Hupp and O. K. Farha, Chem. Commun., 2015, 46, 3501–3510.

15 W. Y. Gao, M. Chrzanowski and S. Ma, Chem. Soc. Rev., 2014, 43, 5841–5866.

16 H. J. Son, S. Jin, S. Patwardhan, S. J. Wezenberg, N. C. Jeong, M. So, C. E. Wilmer, A. A. Sarjeant, G. C. Schatz and R. Q. Snurr, J. Am. Chem. Soc., 2013, 135, 862–869.

17 X.-S. Wang, C.-H. Chen, F. Ichihara, M. Oshikiri, J. Liang, L. Li, Y. Li, H. Song, S. Wang, T. Zhang, Y.-B. Huang, R. Cao and J. Ye, Appl. Catal., B, 2019, 253, 323–330.

18 S. Wu, X. Xing, D. Wang, J. Zhang, J. Chu, C. Yu, Z. Wei, M. Hu, X. Zhang and Z. Li, ACS Sustainable Chem. Eng., 2020, 8, 148–153.

19 X. Deng, L. Yang, H. Huang, Y. Yang, S. Feng, M. Zeng, Q. Li and D. Xu, Small, 2019, 15, 1902287.

20 K. Li, B. Peng and T. Peng, ACS Catal., 2016, 6, 7485–7527.

21 M. Marszewski, S. Cao, J. Yu and M. Jaroniec, Mater. Horiz., 2015, 2, 261–278.

22 L. Shi, T. Wang, H. Zhang, K. Chang and J. Ye, Adv. Funct. Mater., 2015, 25, 5360–5367.

23 S. Liu, F. Chen, S. Li, X. Peng and Y. Xiong, Appl. Catal., B, 2017, 211, 1–10.

24 S. Cao, J. Low, J. Yu and M. Jaroniec, Adv. Mater., 2015, 27, 2150–2176.

25 S. Zhang, P. Gu, R. Ma, C. Luo, T. Wen, G. Zhao, W. Cheng and X. Wang, Catal. Today, 2019, 335, 65–77.

26 Y. Fang, Y. Xu, X. Li, Y. Ma and X. Wang, Angew. Chem., Int. Ed., 2018, 57, 9749–9753.

This journal is © The Royal Society of Chemistry 2020

J. Mater. Chem. A, 2020, 8, 6034–6040 | 6039

27 R. Wang, L. Gu, J. Zhou, X. Liu, F. Teng, C. Li, Y. Shen and Y. Yuan, *Adv. Mater. Interfaces*, 2015, **2**, 1500037.

28 Y. Li, F. Wei, Y. Liu, H. Zhao, X.-N. Ren, J. Liu, T. Hasan, L. Chen and B.-L. Su, *Nanoscale*, 2018, **10**, 4515–4522.

29 J. Zhang, M. Zhang, C. Yang and X. Wang, *Adv. Mater.*, 2014, **26**, 4121–4126.

30 S. R. Lingampalli, M. M. Ayyub and C. N. R. Rao, *ACS Omega*, 2017, **2**, 2740–2748.

31 C.-C. Wang, X.-H. Yi and P. Wang, *Appl. Catal., B*, 2019, **247**, 24–48.

32 M. Tahir, C. Cao, F. K. Butt, F. Idrees, N. Mahmood, Z. Ali, I. Aslam, M. Tanveer, M. Rizwan and T. Mahmood, *J. Mater. Chem. A*, 2013, **1**, 13949–13955.

33 J. Zhang, M. Zhang, R. Q. Sun and X. Wang, *Angew. Chem., Int. Ed.*, 2012, **51**, 10145–10149.

34 S. N. Habisreutinger, L. Schmidt-Mende and J. K. Stolarczyk, *Angew. Chem., Int. Ed.*, 2013, **52**, 7372–7408.